Standard Model is best model (working title)

William Kennedy DiClemente

A DISSERTATION

in

Physics and Astronomy

Presented to the Faculties of The University of Pennsylvania

in Partial Fulfillment of the Requirements for the Degree of Doctor of Philosophy

2018 Last compiled: December 27, 2018

I. Joseph Kroll, Professor, Physics

Supervisor of Dissertation

Joshua Klein, Professor, Physics

Graduate Group Chairperson

Dissertation Committee

(Committee Prof. 1), Professor, Physics

(Committee Prof. 2), Associate Professor, Physics

(Committee Prof. 3), Professor, Physics

(Committee Prof. 4), Professor, Physics

I. Joseph Kroll, Professor, Physics

Standard Model is best model (working title)

Acknowledgements

I'd like to thanks the Ghosts of Penn Students Past for providing me with such an amazing thesis template.

ABSTRACT

STANDARD MODEL IS BEST MODEL (WORKING TITLE)

William Kennedy DiClemente

J. Kroll

This is the abstract text.

Contents

List of Tables

List of Figures

Preface

This is the preface. It's optional, but it's nice to give some context for the reader and stuff.

Will K. DiClemente
Philadelphia, February 2019

Chapter 1

Introduction

The Standard Model (SM)[1] has been remarkably successful...

[1] Here's a footnote.

Chapter 2

Theoretical Framework

(Some example introductory text for this chapter)...

2.1 Introduction to the Standard Model

Modern particle physics is generally interpreted in terms of the Standard Model (SM). This is a quantum field theory which encapsulates our understanding of the electromagnetic, weak, and strong interactions...

2.2 Electroweak Mixing and the Higgs Field

When the theory of the electroweak interaction was first developed [1, 2], the W and Z bosons were predicted to be massless (a typical mass term in the Lagrangian would violate the SU(2) symmetry). However, these were experimentally observed to have masses...

Chapter 3

LHC and the ATLAS Detector

3.1 The Large Hadron Collider

The Large Hadron Collider (LHC) [3] is...

3.2 The ATLAS Detector

ATLAS is a general-purpose particle detector...

3.2.1 The Inner Detector

The Inner Detector serves the primary purpose of measuring the trajectories of charged particles...

3.2.1.1 Pixel Detector

The Pixel detector consists of four cylindrical barrel layers and three disk-shaped endcap layers...

3.2.1.2 Semiconductor Tracker

The Semiconductor Tracker uses the same basic technology as the Pixels, but the fundamental unit of silicon is a larger “strip”...

3.2.1.3 Transition Radiation Tracker

The Transition Radiation Tracker is the outermost component of the ID...

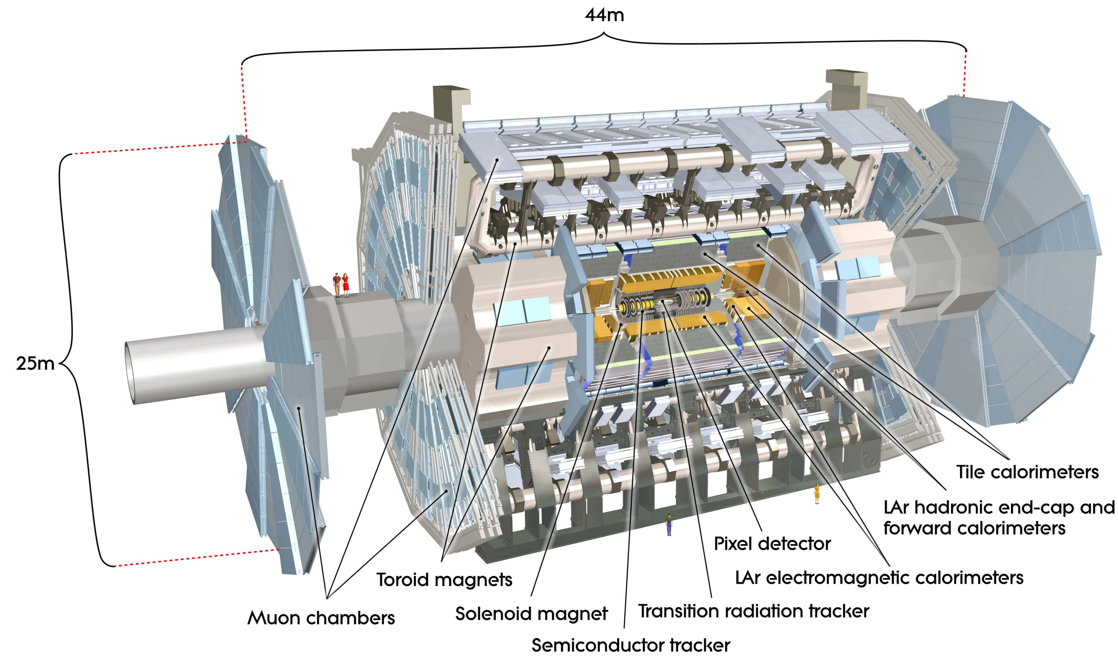

Figure 3.1: General cut-away view of the ATLAS detector [4].

3.2.2 The Calorimeters

ATLAS includes two types of calorimeter system for measuring electromagnetic and hadronic showers. These are the Liquid Argon (LAr) calorimeters and the Tile calorimeters. Together, these cover the region with $|\eta| < 4.9$...

3.2.2.1 Liquid Argon Calorimeters

The Liquid Argon system consists of...

3.2.2.2 Tile Calorimeters

The Tile calorimeter provides coverage for hadronic showers...

Chapter 4

Alignment of the ATLAS Inner Detector

In order for the subdetectors of the ID to operate at their designed precisions, it is essential that the locations of the sensors be known as precisely as possible. Differences between the expected and actual positions of a sensor can result in displaced particle hits and degrade track reconstruction quality. These misalignments can occur for any number of reasons, including but not limited to elemnts shifting during maintenance periods or cycles in ATLAS's magnetic field, or simply small movements during normal detector operations. Since it is not practical to physically realign hundreds of thousands of detector elements to μm precision by hand, an iterative track-based alignment algorithm is used to determine the physical positions and orientations of these elements [5]. The effects of misalignments and the steps taken to correct and monitor them are detailed in this chapter.

4.1 Effects of Misalignment

Hello world!

4.2 The Alignment Method

Hello world!

4.3 Momentum Bias Corrections

Hello world!

4.4 Alignment of the IBL

Hello world!

4.5 Alignment Monitoring

Hello world!

Chapter 5

WZ production @ $\sqrt{s} = 13$ TeV

5.1 Theoretical motivation

Hello world!

5.2 Signal definition

Hello world!

5.3 Background estimations

Hello world!

5.4 Cross section measurement

Hello world!

Chapter 6

Same-sign WW @ $\sqrt{s} = 13$ TeV

6.1 Theoretical motivation

Hello world!

6.2 Signal definition

Hello world!

6.3 Background estimations

Hello world!

6.4 Cross section measurement

Hello world!

Chapter 7

Prospects for same-sign WW at the High Luminosity LHC

On December 3, 2018, Run 2 of the LHC officialy ended, and the collider was shut down to begin the first of two scheduled extended maintenance periods [6]. During these two long shutdowns, the Phase-I and Phase-II upgrades of the LHC and ATLAS will occur in order to prepare for the High-Luminosity LHC (HL-LHC) which is scheduled to begin operation in 2026 [7].

The HL-LHC is planned to run at an instantaneous luminosity of $\mathcal{L} = 5 \times 10^{34}$ cm^{-2}s^{-}1 with an average of 140 collisions per beam-crossing. Over the course of operation, the HL-LHC is expected to collect a total integrated luminosity of $\mathcal{L} = 3000$ fb^{-1} by 2035 [8].

These run conditions are much harsher than what ATLAS has experienced so far, and as a result there are several planned upgrades to the detector. Most notably, the entire ID will be replaced with an all-silicon tracker which will extend the coverage from $|\eta| \leq 2.7$ up to $|\eta| \leq 4.0$. This will allow for reconstruction of charged particle tracks which can in turn be matched to clusters in the calorimeters for electron identification or forward jet tagging [9].

TODO: Why are we studying ssww at the HL-LHC

7.1 Theoretical motivation

The theoretical motivation for studying the ssWW process is detailed in Section 6.1.

7.2 Signal definition

Hello world!

TODO: Add table for full lepton (pre-)selection, full jet (pre-)selection, and then finally the overall event selection

Selection requirement	Selection value
Lepton kinematics	$p_{\mathrm{T}} > 25$ GeV $\lvert\eta\rvert \leq 4.0$
Jet kinematics	$p_{\mathrm{T}} > 30$ GeV for $\lvert\eta\rvert \leq 4.5$ $p_{\mathrm{T}} > 70$ GeV for $\lvert\eta\rvert > 3.8$
Dilepton charge	Exactly two signal leptons with same charge
Dilepton separation	$\Delta R_{l,l} \geq 0.3$
Dilepton mass	$m_{ll} > 20$ GeV
Z boson veto	$\lvert m_{ee} - m_Z\rvert > 10$ GeV (ee-channel only)
$E_{\mathrm{T}}^{\mathrm{miss}}$	$E_{\mathrm{T}}^{\mathrm{miss}} > 40$ GeV
Jet selection	At least two jets with $\Delta R_{l,j} > 0.3$
b jet veto	$N_{\text{b-jet}} = 0$
Dijet separation	$\Delta\eta_{j,j} > 2.5$
Trilepton veto	No additional preselected leptons
Dijet mass	$m_{jj} > 500$ GeV
Lepton-jet centrality[2]	$\zeta > 0$

Table 7.1: derp

7.2.1 Sensitivity to longitudinal polarization

7.3 Background estimations

Hello world!

7.4 Selection optimization

As mentioned earlier, the HL-LHC will feature forward tracking, an increase in center of mass energy, and a higher integrated luminosity. Therefore, this study is an excellent time to see if there are new optimizations to the signal event selection that can improve the signal to background ratio.

7.4.1 Random grid search algorithm

The chosen method for optimizing the event selection is a cut-based algorithm known as the Random Grid Search (RGS) [10]. Consider a simple case of two variables x and y chosen to differentiate the signal from the background. In order to be considered a signal event, a given event would be required to pass a *cut point* $c = \{x > x_c, y > y_c\}$. A simple method to choose the optimal cut point (i.e. the "best" values of the cuts x_c and y_c) would be to construct an $n \times m$ rectangular grid in x and y consisting of points $(x_0, y_0), (x_1, y_1), ..., (x_n, y_m)$, as in Figure 7.1. One can then choose a cut point $c_k = \{x > x_i, y > y_j\}$ that maximizes the signal significance as measured by a chosen metric. This would be considered a *regular* or *rectangular* grid search.

While effective in principle, this rectangular grid search comes with two major drawbacks:

1. The algorithm does not scale well as the number of variables to be optimized–the dimensionality of the grid–increases. In the case of a square grid with N bins per variable v, the number of cut points to be evaluated grows as N^v.

2. Signal and background samples are rarely evenly distributed over the entire grid, resulting in many cut points being sub-optimal and evaluating them would be a waste of computing resources.

To combat these limitations, the RGS algorithm constructs a grid of cut points directly from the signal sample itself. In the two-dimensional example, this means that the variables x_i and y_j making up the cut point $c_k = \{x > x_i, y > y_j\}$ take their values directly from a given signal event. This has the benefit of creating a *random grid* of cut points that is by construction biased towards regions of high signal concentration. This reduces the need for exponentially increasing numbers of cut points while ensuring that computing resources are not wasted in regions with few to no signal events. An example of the the two-dimensional random grid is shown in Figure 7.2.

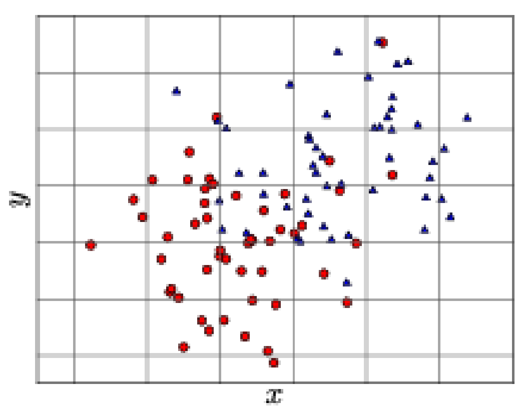

Figure 7.1: A visual representation of a rectangular grid search algorithm. The signal events are the blue triangles, and the red circles are the background events. TODO: replace with own figure

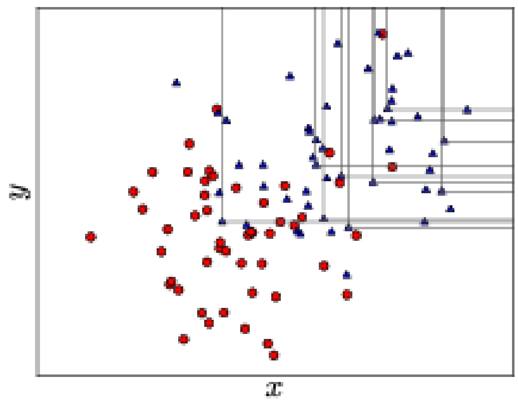

Figure 7.2: A visual representation of a random grid search algorithm. The signal events are the blue triangles, and the red circles are the background events. TODO: replace with own figure

Once the random grid of cut points is constructed, the optimal cut point can be chosen using whatever metric the analyzer chooses, such as signal to background ratio. For the purpose of the $W^{\pm}W^{\pm}jj$ upgrade study, the optimal cut point is the one that mazimizes the signal significance Z defined as in Equation 7.1 [11].

$$Z = \sqrt{2\left[(s+b)\ln\left(\frac{s+b}{b_0}\right) + b_0 - s - b\right] + \frac{(b-b_0)^2}{\sigma_b^2}} \tag{7.1}$$

where s and b are the number of signal and background events, respectively, σ_b is the total uncertainty on the background, and b_0 is defined as:

$$b_0 = \frac{1}{2}\left(b - \sigma_b^2 + \sqrt{(b-\sigma_b^2)^2 + 4(s+b)\sigma_b^2}\right) \tag{7.2}$$

In the case where the backround is known precisely (i.e. $\sigma_b = 0$), Equation 7.1 simplifies to

$$Z = \sqrt{2\left(b\big[(1+s/b)\ln(1+s/b) - s/b\big]\right)} \tag{7.3}$$

which further reduces to the familiar $Z = s/\sqrt{b}$ for the case when $s << b$.

7.4.2 Inputs to the optimization

In order to train the RGS, signal and background samples were prepared from events passing the event selection outlined in Table 7.1 up through the b-jet veto. The signal sample was chosen to be the longitudinally polarized $W^{\pm}W^{\pm}jj$ EWK events, and the transverse and mixed polarizations were treated as background along with $W^{\pm}W^{\pm}jj$ events from QCD interactions and the traditional backgrounds listed in Section 7.3. Splitting the inclusive $W^{\pm}W^{\pm}jj$ EWK events by polarization allows the optimization to favor the longitunally polarized events as much as possible, even though they both contribute to the EWK signal.

The following six variables were chosen for optimization:

- Leading lepton p_{T}
- Dilepton invariant mass (m_{ll})
- Leading jet p_{T}
- Subleading jet p_{T}
- Dijet invariant mass (m_{jj})
- Lepton-jet centrality (ζ)

Subleading lepton p_{T} is omitted due to the fact that it is particularly sensitive to the longitudinal polarization and thus would like to be kept as low as possible.

TODO: talk about constraints to optimization, statistical limitations from fakes resulting in using simplified Z Two constraints were applied to the optimization in order to

7.4.3 Results of the optimization

Selection requirement	Selection value
Lepton kinematics	$p_{\mathrm{T}} > 28$ GeV (leading lepton only)
Jet kinematics	$p_{\mathrm{T}} > 90$ GeV (leading jet)
	$p_{\mathrm{T}} > 45$ GeV (subleading jet)
Dilepton mass	$m_{ll} > 28$ GeV
Dijet mass	$m_{jj} > 520$ GeV
Lepton-jet centrality	$\zeta > -0.5$

Table 7.2: Updates to the $W^{\pm}W^{\pm}jj$ event selection criteria after optimization. Cuts not listed remain unchanged from the default selection in Table 7.1.

The results of the optimization including the event yields as well as the cross section measurement are detailed alongside those using the default selection in Section 7.5.

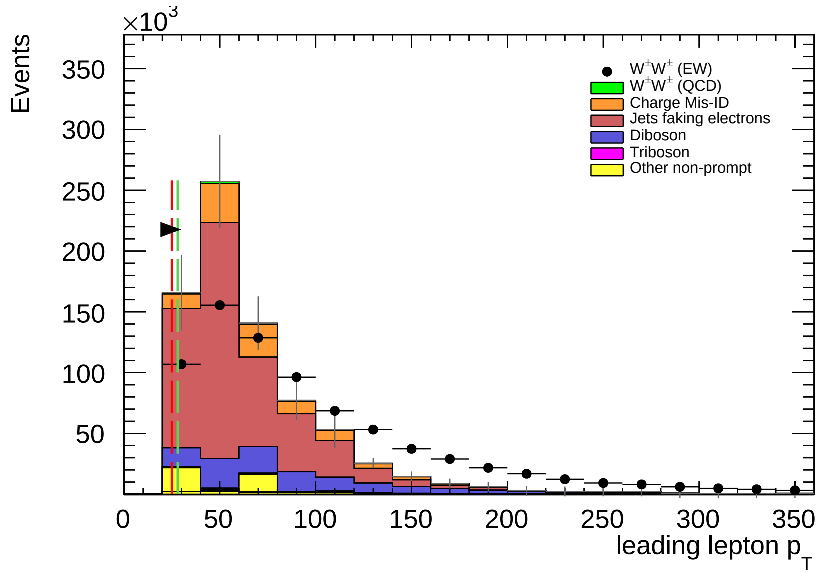

Figure 7.3: Leading lepton p_{T} distribution. The default and optimized cuts are represented by the red and green dashed lines, respectively. The $W^{\pm}W^{\pm}jj$ EWK signal (black points) is normalized to the same area as the sum of the backgrounds (colored histogram).

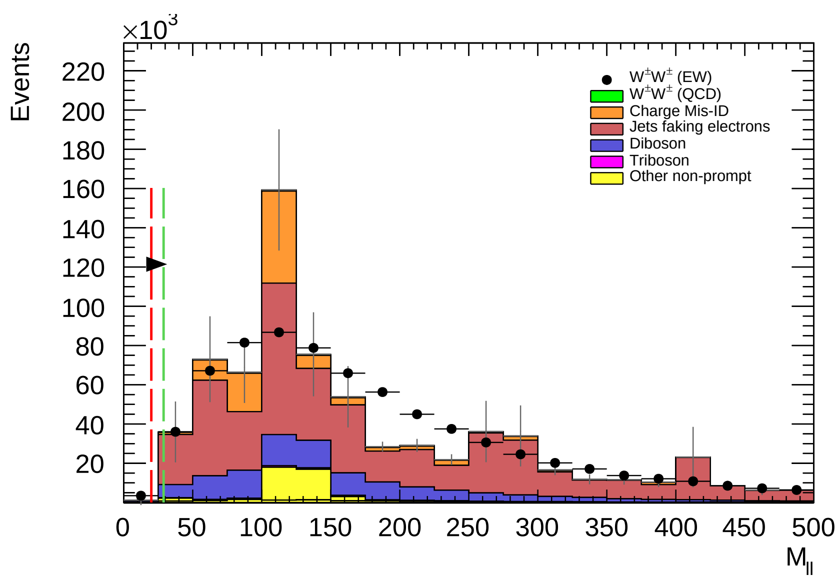

Figure 7.4: Dilepton invariant mass distribution. The default and optimized cuts are represented by the red and green dashed lines, respectively. The $W^{\pm}W^{\pm}jj$ EWK signal (black points) is normalized to the same area as the sum of the backgrounds (colored histogram).

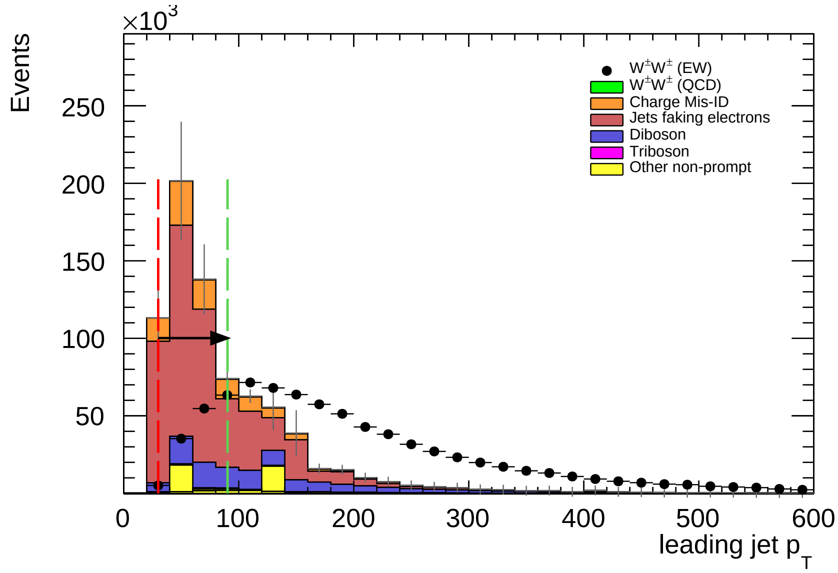

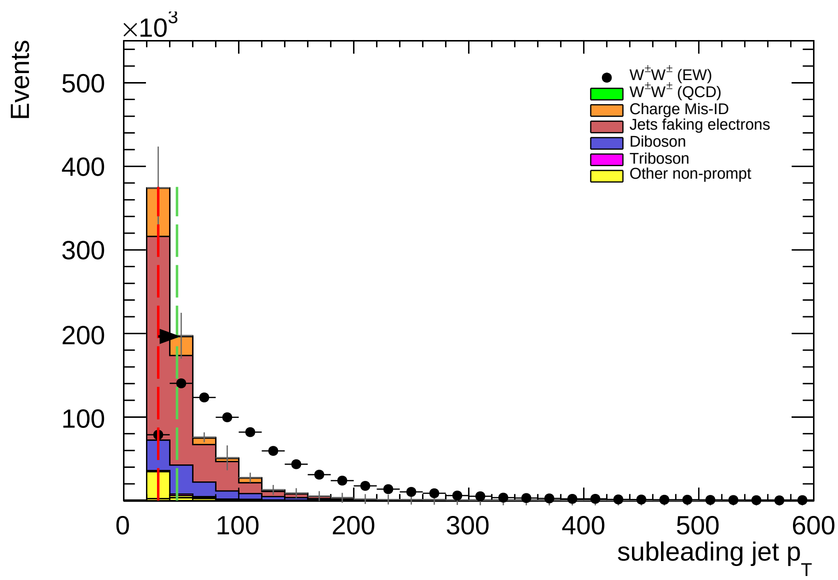

Figure 7.5: Leading (top) and subleading (bottom) jet p_{T} distributions. The default and optimized cuts are represented by the red and green dashed lines, respectively. The $W^{\pm}W^{\pm}jj$ EWK signal (black points) is normalized to the same area as the sum of the backgrounds (colored histogram).

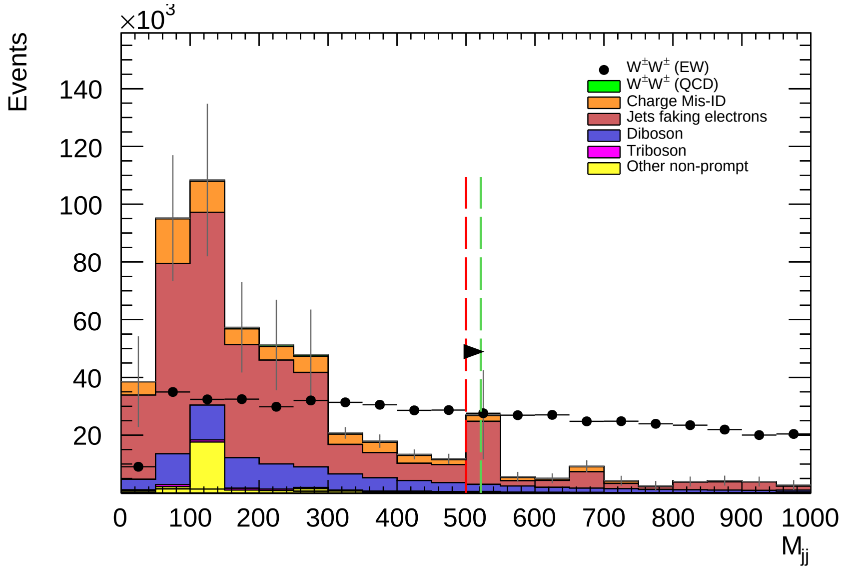

Figure 7.6: Dijet invariant mass distribution. The default and optimized cuts are represented by the red and green dashed lines, respectively. The $W^{\pm}W^{\pm}jj$ EWK signal (black points) is normalized to the same area as the sum of the backgrounds (colored histogram).

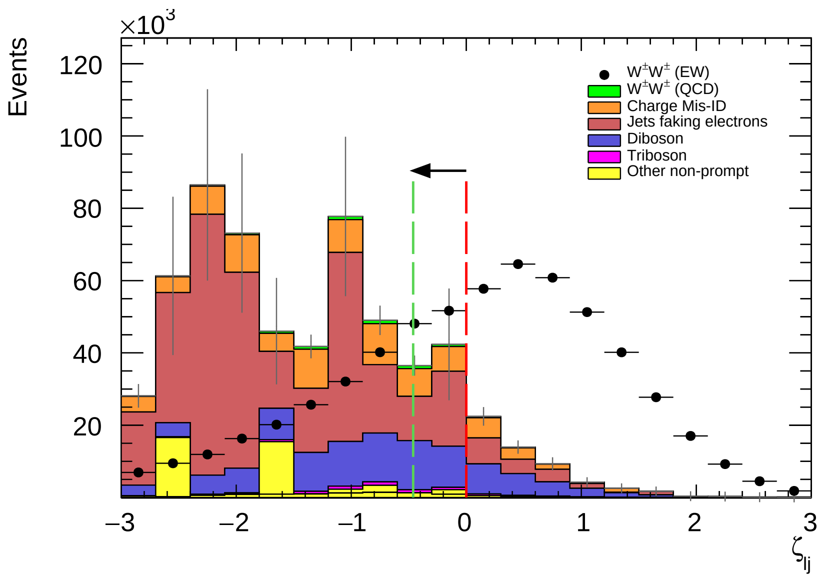

Figure 7.7: Lepton-jet centrality distribution. The default and optimized cuts are represented by the red and green dashed lines, respectively. The $W^{\pm}W^{\pm}jj$ EWK signal (black points) is normalized to the same area as the sum of the backgrounds (colored histogram).

7.5 Results

7.5.1 Event yields

7.5.2 Uncertainties

7.5.3 Cross section measurement

Chapter 8

Conclusion

Here's where you wrap it up.

Looking Ahead

Here's an example of how to have an "informal subsection".

Bibliography

[1] S. L. Glashow, *The Renormalizability of Vector Meson Interactions*, Nucl. Phys. **10** (1959) 107–117. 2.2

[2] A. Salam and J. C. Ward, *Weak and Electromagnetic Interactions*, Nuovo Cimento **11** (1959) 568–577. 2.2

[3] L. R. Evans and P. Bryant, *LHC Machine*, JINST **3** (2008) S08001. https://cds.cern.ch/record/1129806. This report is an abridged version of the LHC Design Report (CERN-2004-003). 3.1

[4] ATLAS Collaboration, *The ATLAS Experiment at the CERN Large Hadron Collider*, JINST **3** (2008) S08003. 3.1

[5] ATLAS Collaboration Collaboration, *Alignment of the ATLAS Inner Detector Tracking System with 2010 LHC proton-proton collisions at $\sqrt{s} = 7$ TeV*, Tech. Rep. ATLAS-CONF-2011-012, CERN, Geneva, Mar, 2011. https://cds.cern.ch/record/1334582. 4

[6] R. Steerenberg, *LHC Report: Another run is over and LS2 has just begun...*, https://home.cern/news/news/accelerators/lhc-report-another-run-over-and-ls2-has-just-begun, 2018. Accessed: 2018-12-14. 7

[7] *Letter of Intent for the Phase-I Upgrade of the ATLAS Experiment*, Tech. Rep. CERN-LHCC-2011-012. LHCC-I-020, CERN, Geneva, Nov, 2011. http://cds.cern.ch/record/1402470. 7

[8] G. Apollinari, I. Bjar Alonso, O. Brning, M. Lamont, and L. Rossi, *High-Luminosity Large Hadron Collider (HL-LHC): Preliminary Design Report*. CERN Yellow Reports: Monographs. CERN, Geneva, 2015. https://cds.cern.ch/record/2116337. 7

[9] ATLAS Collaboration Collaboration, ATLAS Collaboration, *ATLAS Phase-II Upgrade Scoping Document*, Cern-lhcc-2015-020, Geneva, Sep, 2015. http://cds.cern.ch/record/2055248. 7

[10] P. C. Bhat, H. B. Prosper, S. Sekmen, and C. Stewart, *Optimizing Event Selection with the Random Grid Search*, Comput. Phys. Commun. **2**28 (2018) 245–257, arXiv:1706.09907 [hep-ph]. 7.4.1

[11] G. Cowan, K. Cranmer, E. Gross, and O. Vitells, *Asymptotic formulae for likelihood-based tests of new physics*, Eur. Phys. J. **C**71 (2011) 1554, arXiv:1007.1727 [physics.data-an]. [Erratum: Eur. Phys. J.C73,2501(2013)]. 7.4.1